

Journal of Materials Chemistry A

Accepted Manuscript



This is an *Accepted Manuscript*, which has been through the Royal Society of Chemistry peer review process and has been accepted for publication.

Accepted Manuscripts are published online shortly after acceptance, before technical editing, formatting and proof reading. Using this free service, authors can make their results available to the community, in citable form, before we publish the edited article. We will replace this *Accepted Manuscript* with the edited and formatted *Advance Article* as soon as it is available.

You can find more information about *Accepted Manuscripts* in the [Information for Authors](#).

Please note that technical editing may introduce minor changes to the text and/or graphics, which may alter content. The journal's standard [Terms & Conditions](#) and the [Ethical guidelines](#) still apply. In no event shall the Royal Society of Chemistry be held responsible for any errors or omissions in this *Accepted Manuscript* or any consequences arising from the use of any information it contains.



Facile and scalable fabrication of three-dimensional Cu(OH)₂ nanoporous nanorods for solid-state supercapacitors†

Jizhang Chen,^a Junling Xu,^a Shuang Zhou,^a Ni Zhao*^a and Ching-Ping Wong*^{a,b}

Received 00th January 20xx,
Accepted 00th January 20xx

DOI: 10.1039/x0xx00000x

www.rsc.org/

A facile and scalable one-step anodization method has been developed to fabricate three-dimensional (3-D) Cu(OH)₂ nanoporous nanorods on the copper foil substrate, a product that can be used directly as a binder-free electrode for supercapacitors. The unique morphology of the nanorods provides a large amount of active sites for redox reactions, which can be easily accessed by electrolyte ions. Benefiting from that, a high capacitance of 213 mF cm⁻² is obtained, and superior rate capability (62.3% capacitance retention when the scan rate is increased to 10 times) and excellent cyclability (92.0% capacitance retention after 5000 cycles) are achieved. In addition, a flexible and foldable solid-state asymmetric supercapacitor is assembled using the Cu(OH)₂ and activated carbon as the positive and negative electrodes, respectively. The devices deliver a high energy density of 3.68 mWh cm⁻³ and a high power density of 5314 mW cm⁻³, demonstrating a great potential for next-generation high-rate energy storage systems.

Introduction

Currently there are increasing technological demands for supercapacitors, which store and release energy very rapidly with excellent long-term cyclability, and are therefore ideal for high-power applications such as hybrid electrical vehicles, portable electronic devices, cranes and forklifts.¹ Supercapacitors can be classified into non-Faradaic electrical double layer capacitors (EDLCs) and Faradaic pseudocapacitors based on their charge storage mechanisms. EDLCs primarily make use of carbon materials (*e.g.*, activated carbon,² graphene^{3,4}) as the active material and store energy by accumulating charges in the electrostatic double layer. Although EDLCs are able to operate at much higher rates than batteries, their energy densities are considerably lower. An effective approach to enhance their energy densities is to expand the working potential window, since the potential window has a quadratic relationship with the energy density.⁵ As a result, organic and ionic liquid electrolytes have been explored to replace aqueous electrolytes, owing to their much wider potential windows (≥ 2.5 V). However, the use of these nonaqueous electrolytes increases the costs of supercapacitors and is less environmentally friendly.^{2,6} An alternative strategy to enhance the energy density is to construct asymmetric supercapacitors (ASCs) operated in aqueous or gel electrolytes. Usually in such systems, one of the carbon electrodes is replaced by a pseudocapacitive electrode, which can store more charges than carbon electrodes via fast and reversible surface/

near-surface redox reactions. Thus higher energy density can be realized owing to the increased capacitance and widened potential window (~ 1.6 V vs. ~ 1.0 V in aqueous EDLCs).

Recently, transition metal oxides (*e.g.*, MnO₂,⁷⁻¹¹ NiCo₂O₄,¹²⁻¹⁵ Fe₂O₃¹⁶), hydroxides (*e.g.*, Ni(OH)₂,¹⁷⁻¹⁹ layered double hydroxides^{20,21}), sulfides (*e.g.*, NiCo₂S₄,²²⁻²⁵ Ni₃S₂²⁶), and conducting polymers²⁷⁻²⁹ have been explored as potential pseudocapacitive materials. Since their pseudocapacitive activities rely on redox reactions, charge (electron or electrolyte ion) transport within the bulk of these materials is crucial to their performances, especially when their particle sizes are not too low. Unfortunately, most of them suffer from insufficient charge transport, which limits the utilization efficiency of these materials. As a result, the high theoretically predicted pseudocapacitances are seldom obtained in practical experiments. Various approaches have been explored to address this challenge, such as (1) engineering the size, morphology and porosity of the active material, (2) implementing core-shell structures where a nano-conductive core is wrapped with a pseudocapacitive material, and (3) modifying the contact between the active material and current collector. Despite the reported enhancement in the charge storage property, most of these strategies are complex and expensive, making them difficult to scale up for commercialization.

In this work, we focus on Cu(OH)₂, a well-known low-cost, abundant, and non-toxic material, yet rarely explored for supercapacitor applications.³⁰ We have developed a facile, scalable and cost-effective one-step process to anodically grow three-dimensional (3-D) Cu(OH)₂ nanoporous nanorods on the Cu foil. Such product can be directly assembled in a supercapacitor configuration and delivers superior pseudocapacitive performances in both three-electrode and two-electrode measurements. An ASC was fabricated using the Cu(OH)₂ and activated carbon (AC) as the positive and negative electrodes, respectively. The device delivers a

^a Department of Electronic Engineering, The Chinese University of Hong Kong, New Territories, Hong Kong. E-mail: nzhao@ee.cuhk.edu.hk (N. Zhao), cpwong@cuhk.edu.hk (C. Wong).

^b School of Materials Science and Engineering, Georgia Institute of Technology, Atlanta, Georgia 30332, United States.

† Electronic Supplementary Information (ESI) available: Calculations, supplementary figures and supplementary video. See DOI: 10.1039/x0xx00000x

high energy density of 3.68 mWh cm^{-3} at a high power density of 1253 mW cm^{-3} , demonstrating a great potential for commercial applications.

Experimental section

Fabrication of 3-D $\text{Cu}(\text{OH})_2$

Copper foils were purchased from Shenzhen Bright Copper Co., Ltd. and used before immersion in diluted HCl solution. The Cu foil was cut into $2 \times 3 \text{ cm}^2$ slices with one side covered by the insulation tape. 3-D $\text{Cu}(\text{OH})_2$ was fabricated by an anodization process in 1 M NaOH aqueous solution at room temperature. A constant current of 1.5 mA cm^{-2} was applied for 1800 s in a two electrode setup, using the $2 \times 3 \text{ cm}^2$ Cu slice as the working electrode and a $0.5 \times 0.5 \text{ cm}^2$ Pt plate as the reference electrode. During the anodization, about $2 \times 2 \text{ cm}^2$ area of the Cu slice was immersed in the solution as the deposition zone. After the anodization, the as-obtained Cu slice with nanostructured $\text{Cu}(\text{OH})_2$ was used directly as the binder-free electrode for electrochemical measurements. No additional washing step is required. The mass loading of $\text{Cu}(\text{OH})_2$ on the Cu slice was determined by the weight difference of the $\text{Cu}(\text{OH})_2/\text{Cu}$ slice before and after immersion in diluted HCl solution.

Characterization and electrochemical measurements

The XRD patterns were collected using a Rigaku (RU300) diffractometer with Cu K α radiation source ($\lambda = 0.1540598 \text{ nm}$). The chemical composition was investigated using X-ray photoelectron spectroscopy (XPS, Physical Electronics PHI 5600). N_2 adsorption/desorption measurement was carried out by Micromeritics ASAP 2010 instrument. The morphology and microstructure of the electrode materials were characterized by a field emission scanning electron microscope (FE-SEM, Quanta F400) and a transmission electron microscope (TEM, Tecnai F20).

The as-obtained $2 \times 3 \text{ cm}^2$ Cu slice was cut in half with each Cu slice ($1 \times 3 \text{ cm}^2$) possessing a $1 \times 2 \text{ cm}^2$ zone of $\text{Cu}(\text{OH})_2$. Three-electrode measurements were performed using the $\text{Cu}(\text{OH})_2/\text{Cu}$ slice, $0.5 \times 0.5 \text{ cm}^2$ Pt plate, saturated calomel electrode (SCE) and 1 M NaOH aqueous solution as the working electrode, counter electrode, reference electrode and electrolyte, respectively. Cyclic voltammetry (CV) and galvanostatic charging/discharging (GCD) tests were conducted at different scan rates and current densities (based on the mass of $\text{Cu}(\text{OH})_2$) on a CHI 660E electrochemical workstation on 1×3 and $2 \times 3 \text{ cm}^2$ $\text{Cu}(\text{OH})_2/\text{Cu}$ slices, respectively. For the two-electrode measurements, a solid-state ASC device was assembled by using the $1 \times 3 \text{ cm}^2$ $\text{Cu}(\text{OH})_2/\text{Cu}$ slice, $1 \times 3 \text{ cm}^2$ activated carbon (AC) electrode and polyvinyl alcohol (PVA)/KOH gel as the positive electrode, negative electrode and electrolyte/separator, respectively. The mass ratio between $\text{Cu}(\text{OH})_2$ and AC was estimated according to the charge balance: $q_+ = q_-$. The AC electrode was prepared by mixing AC with polyvinylidene difluoride (PVDF) and Super P (conductive carbon black) at a weight ratio of 8:1:1 and then pasting the slurry onto $1 \times 3 \text{ cm}^2$ Cu foils (the pasted zone is $1 \times 2 \text{ cm}^2$), followed by vacuum drying at 100°C for 12 h. The PVA/KOH gel electrolyte was prepared by adding 2 g PVA power and 1.12 g KOH to 20 mL deionized water and heating this mixture to 85°C under vigorous stirring until the solution became clear. The obtained viscous solution was dropped onto $\text{Cu}(\text{OH})_2$ and AC

electrodes (both $1 \times 3 \text{ cm}^2$), and then these two electrodes were assembled together. After the electrolyte solidified to a gel, the two electrodes were further pressed to form a $1 \times 4 \text{ cm}^2$ device with the effective area being around 2 cm^2 . GCD tests were carried out at different current densities based on the total mass of $\text{Cu}(\text{OH})_2$ and AC.

Results and discussion

One-step electrochemical anodization was performed to grow 3-D $\text{Cu}(\text{OH})_2$, as shown in Fig. 1. The anodization was carried out on a Cu foil in 1 M NaOH aqueous solution under a constant current for 1800 s. During the anodization, Cu atoms on the surface of the Cu foil are oxidized to Cu^{2+} , which subsequently react with OH^- and grow into 3-D $\text{Cu}(\text{OH})_2$ onto the surface of the Cu foil. As shown by photographs, the surface colour of the Cu foil turned from red-orange into blue-green after the anodization, suggesting the conversion of Cu to $\text{Cu}(\text{OH})_2$ on the foil surface. The growth of $\text{Cu}(\text{OH})_2$ is also evidenced by X-ray diffraction (XRD), which reveals the formation of orthorhombic $\text{Cu}(\text{OH})_2$ (JCPDS 13-0420, space group *Cmcm*) after anodization. No XRD features are observed for other oxidation states of Cu, demonstrating a relatively high purity of the $\text{Cu}(\text{OH})_2$ phase. It is worth noting that our fabrication process utilizes low-cost raw materials and requires no pre- or post-treatments for the anodization growth step. Such a facile and cost-effective fabrication process renders our product realistic and competitive for practical applications.

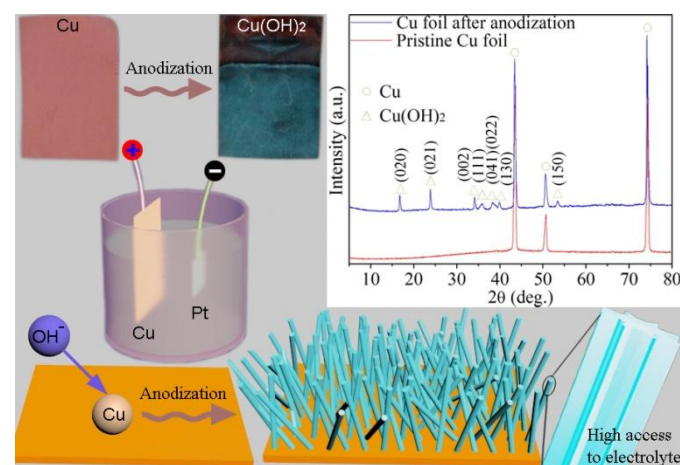


Fig. 1 Illustration of the fabrication process of 3-D $\text{Cu}(\text{OH})_2$. The inset shows photographs and XRD patterns of the Cu foil before and after the anodization.

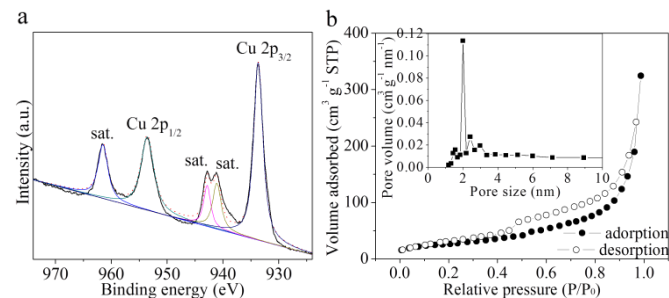


Fig. 2 (a) High-resolution core level Cu 2p XPS spectrum and (b) N_2 adsorption and desorption isotherm of 3-D $\text{Cu}(\text{OH})_2$. The inset shows corresponding BJH pore-size distribution.

The chemical composition and purity of 3-D Cu(OH)₂ were further investigated by X-ray photoelectron spectroscopy (XPS). As shown in Fig. 2a, the high-resolution XPS spectrum for the Cu 2p core level shows two distinct peaks at 953.5 and 933.7 eV, corresponding to a spin-orbit couple of Cu 2p_{1/2} and Cu 2p_{3/2}. These two peaks together with their shake-up satellites at 961.5, 942.8 and 941.1 eV are characteristic of d⁹ Cu(II) compounds.³¹ In addition, survey XPS spectrum of 3-D Cu(OH)₂ is depicted in Fig. S1, confirming high purity of this product. Fig. 2b shows N₂ adsorption/desorption isotherm of 3-D Cu(OH)₂, displaying a type IV (IUPAC classification) isotherm with a large H3-type (IUPAC classification) hysteresis loop. These characteristics are indicative of sufficient nanopores, which can also be confirmed by the Barrett-Joyner-Halenda (BJH) pore-size distribution in the inset of Fig. 2b. Brunauer-Emmett-Teller (BET) specific surface area of 3-D Cu(OH)₂ is calculated to be 94.7 m² g⁻¹ based on this isotherm.

Fig. 3 shows electron microscopic images of the anodically grown Cu(OH)₂. It can be seen that the Cu(OH)₂ nanorods have a diameter of ~200 nm. These nanorods are not perpendicular to the substrate, but slant randomly, demonstrating a 3-D structure. It is also found from Fig. 3b that the cross-section of the Cu(OH)₂ nanorods is neither circular nor hexagonal, but adopts a concave polygon shape with corners extended outwards, beneficial for maximizing the contact area between Cu(OH)₂ and the electrolyte. In addition, these anodically fabricated Cu(OH)₂ nanorods grow uniformly on the Cu slice, as shown by the low-magnification SEM images in Fig. S2. The thickness of Cu(OH)₂ grown on the Cu coil is estimated to be 6.3–8.1 μm based on the cross-section image in Fig. 3c. The TEM images (Fig. 3d,e and Fig. S3) of Cu(OH)₂ reveal a nanoporous structure of the nanorods, which may help to reduce the electrode impedance and enhance the pseudocapacitance by facilitating ionic diffusion to the redox active sites.^{17,32,33} The inset of Fig. 3e shows a high-resolution TEM image of Cu(OH)₂, which exhibits fringes with a lattice spacing of 0.265 nm, in good agreement with the (040) plane of Cu(OH)₂.

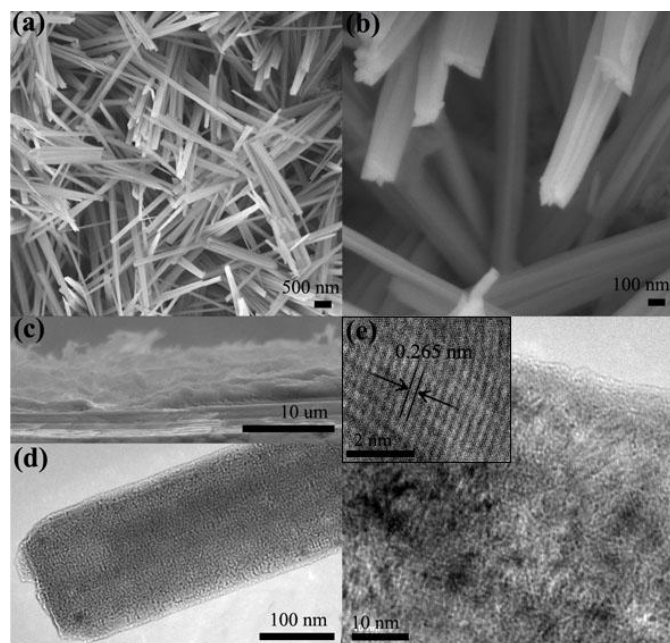


Fig. 3 (a-c) SEM images and (d,e) TEM images of 3-D Cu(OH)₂.

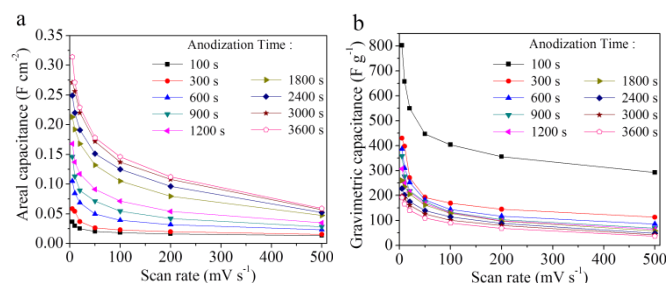


Fig. 4 (a) Areal and (b) gravimetric capacitances of 3-D Cu(OH)₂ with respect to the different anodization time, plotted vs. the scan rate.

Besides 1800 s, we have applied various anodization time to the growth of 3-D Cu(OH)₂. The mass loadings of Cu(OH)₂ on the Cu slice under different anodization time are plotted in Fig. S4 and fitted. According to the fitting result, the mass loadings are 0.0454, 0.8177 and 1.6354 mg/cm² when the anodization time is 100, 1800 and 3600 s, respectively. SEM images of the Cu(OH)₂ obtained under different anodization time are exhibited in Fig. S5. When the anodization time is 100 s, Cu(OH)₂ shows a morphology of short nanorods (the background humps are from the Cu substrate). When the time is 1800 s, these nanorods become much longer and much denser. When the time is increased to 3600 s, the diameter of these nanorods becomes much larger. Cyclic voltammetry (CV) measurements were conducted in a three-electrode configuration to explore the influence of the anodization time on the performance of the Cu(OH)₂. Fig. 4 summarizes the scan rate-dependent areal and gravimetric capacitances (C_a and C_g , see the calculation in Supporting Information) of Cu(OH)₂ with an anodization time varying from 100 to 3600 s. When the anodization time is 100, 1800 and 3600 s, C_a are 0.036, 0.213 and 0.314 F cm⁻² at 5 mV s⁻¹ and 0.020, 0.132 and 0.178 F cm⁻² at 50 mV s⁻¹, respectively, while C_g are 802, 260 and 192 F g⁻¹ at 5 mV s⁻¹ and 447, 162 and 109 F g⁻¹ at 50 mV s⁻¹, respectively. It can be seen that (1) when the anodization time is decreased, C_a drops down while C_g goes up; and (2) when the scan rate is increased, both C_a and C_g decrease. The former point indicates that the performance of Cu(OH)₂ is greatly influenced by the anodization time, which corresponds to the mass loading of Cu(OH)₂ onto the Cu foil. The longer anodization time increases the mass loading and leads to larger C_a . However, the higher mass loading also induces an increase in the diameter and length of the Cu(OH)₂ nanorods. This leads to a lower C_g since only the surface/near-surface layer of Cu(OH)₂ that is close to the Cu substrate is electrochemically active. The latter point reveals a phenomenon of electrochemical polarization. At low scan rates, electrolyte ions and electrons are provided with sufficient time to access the interior reaction sites of Cu(OH)₂. Whereas at high scan rates, the movements of charges within Cu(OH)₂ cannot be synchronized with the rapid transfer of electrons in the external circuit. Hence the capacitance decreases with the increase of the scan rate.

Given that 1800 s anodization time gives a balanced performance between C_a and C_g , hereafter we focus on the 1800 s Cu(OH)₂, whose CV curves are shown in Fig. 5a. These CV profiles are quite different from the ideal rectangular shape of EDLCs, implying that charging/discharging of Cu(OH)₂ is dominated by a Faradaic process:

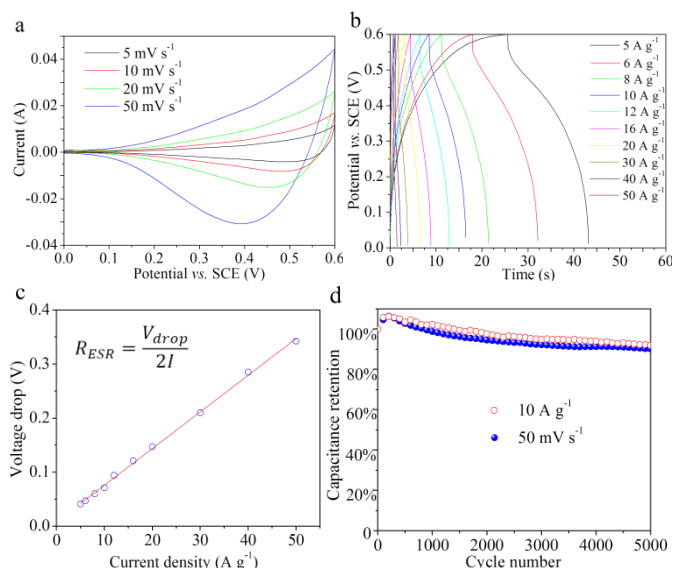


Fig. 5 Electrochemical performances of 3-D Cu(OH)₂ (1800 s) evaluated in a three electrode setup. (a) CV curves at different scan rates. (b) GCD profiles at different current densities. (c) Voltage drops during GCD tests, plotted vs. the current density. (d) Cycling performances under CV and GCD tests.

$2\text{Cu}(\text{OH})_2 + 2\text{e}^- \leftrightarrow 2\text{CuOH} + 2\text{OH}^- \leftrightarrow \text{Cu}_2\text{O} + \text{H}_2\text{O} + 2\text{OH}^-$. The anodic peaks are not distinct, while broad cathodic peaks move from 0.51 to 0.50, 0.47 and 0.41 V as the scan rate is increased from 5 to 10, 20 and 50 mV s⁻¹, respectively. These profiles are very similar to those of previously reported CuO.^{34,35} In order to find why anodic peaks are not distinct, we investigated CV curves of the Cu(OH)₂ under different potential cutoffs, as shown in Fig. S6. It is found that: (1) water splitting is negligible under 0.6 V cutoff, since the current response of the neat Cu slice under this cutoff is very low; (2) typical behaviour of water splitting is observed when the potential cutoff is higher than 0.6 V; (3) the cathodic peak current rises when the potential cutoff is increased, and the largest rises are observed when the potential cutoff is increased from 0.6 to 0.7 V and from 0.7 to 0.8 V. These results indicate the anodic peak arising from Cu(I) to Cu(II) may locate at around 0.7 V that overlaps with the potential where water splits, and as a result, the anodic peaks are not distinct due to the incomplete conversion between Cu(I) and Cu(II) and the influence of water splitting. In case of the broad nature of cathodic peaks, this phenomenon is caused by (1) incomplete conversion between Cu(I) and Cu(II) and (2) high scan rates used here.

Galvanostatic charging/discharging (GCD) curves of the Cu(OH)₂ at different current densities are presented in Fig. 5b. These curves are observed to deviate from the typical triangular shape of EDLCs, reflecting again the dominant pseudocapacitive characteristic of Cu(OH)₂. In addition, these GCD curves show near-symmetric characteristic, revealing great redox reversibility. When the current density reaches 10 A g⁻¹, the Cu(OH)₂ still maintains a large discharging capacitance of 133.3 F g⁻¹ or 123.7 mF cm⁻², manifesting excellent rate capability that is suitable for high-power applications. Normally, abrupt voltage drops are observed at the beginning of the discharging curves, due to the equivalent series resistance (R_{ESR}) of the testing system, which consists of the intrinsic resistance of

the active material, the contact resistance of the active material and current collector and the ionic resistance from the electrolyte. Herein the average R_{ESR} is calculated to be merely 0.284 Ω cm⁻² through all current densities (Fig. 5c). Such a low R_{ESR} is attributed to the following two factors. Firstly, since Cu(OH)₂ grows directly from Cu, an excellent contact is formed between the two materials. Secondly, the conductivity of the Cu substrate, which serves as the current collector, is very high. The 3-D Cu(OH)₂ was further tested at 50 mV s⁻¹ and 10 A g⁻¹ for cyclability, as shown in Fig. 5d. It is seen that it maintains 90.1% and 92.0% of its initial capacitance even after 5000 cycles under CV and GCD tests, respectively. Interestingly, the morphology of Cu(OH)₂ keeps unchanged after these cycles (see Fig. S7), implying great structural stability of 3-D Cu(OH)₂. In addition to such excellent electrochemical stability, the performance of our product 3-D Cu(OH)₂ surpasses many recently reported pseudocapacitive materials (see the comparison in Table 1), such as MoS₂ nanoporous film (14.5 mF cm⁻²),³⁶ Ni(OH)₂ thin-film (70.6 mF cm⁻²),¹⁷ MnO₂/CNT film (100 mF cm⁻²),⁷ MnMoO₄/CoMoO₄ nanowires (134.7 F g⁻¹),³⁷ O-deficient Fe₂O₃ nanorods (89 F g⁻¹),³⁸ and various Cu-based materials. The superior electrochemical properties of 3-D Cu(OH)₂ can be ascribed to the following two reasons: (1) the unique morphology and porous structure of 3-D Cu(OH)₂ provide a large contacting area with the electrolyte and therefore maximize the number of active sites for surface redox reaction; (2) the direct growth of Cu(OH)₂ on the Cu slice (the current collector) reduces the interfacial contact resistance and enhances charge transport. It should also be noted that the substrate for the anodization is not limited to the Cu foil. Other substrates such as metal wires, carbon cloths, and polymer films can also be used for the anodic formation of 3-D Cu(OH)₂, as long as a pre-treatment such as electroless-plating of Cu is performed.

Table 1 Comparison of 3-D Cu(OH)₂ (1800 s) with recently reported pseudocapacitive materials.

| Active material | Electrolyte | Capacitance | Ref. |
|---|---------------------------------------|---|------|
| 3-D Cu(OH) ₂ in this work | 1 M NaOH | 213 mF cm ⁻² , 260 F g ⁻¹ at 5 mV s ⁻¹ 168 mF cm ⁻² at 20 mV s ⁻¹ 147.5 F g ⁻¹ at 5 A g ⁻¹ | |
| TiO ₂ nanotube film | 1 M KCl | 0.911 mF cm ⁻² at 1 mV s ⁻¹ | 43 |
| AuPd@MnO ₂ nanopillars | 1M Na ₂ SO ₄ | 6.13 mF cm ⁻² at 5 mV s ⁻¹ | 9 |
| Fe ₃ O ₄ @SnO ₂ nanorod film | 1 M Na ₂ SO ₄ | 7.0 mF cm ⁻² at 0.2 mA cm ⁻² | 44 |
| Ni@NiO inverse opal | 1 M KOH | 11 mF cm ⁻² at 0.2 mA cm ⁻² | 45 |
| MoS ₂ nanoporous film | 0.5 M H ₂ SO ₄ | 14.5 mF cm ⁻² at 1 mA cm ⁻² | 36 |
| WO _{3-x} @Au@MnO ₂ nanowires | 0.1M Na ₂ SO ₄ | 294 mF cm ⁻² at 10 mV s ⁻¹ | 46 |
| Cu(OH) ₂ thin film | 1 M NaOH | 34 mF cm ⁻² at 10 mV s ⁻¹ | 30 |
| SnO ₂ @MnO ₂ nanowires | 1 M Na ₂ SO ₄ | 50.96 mF cm ⁻² at 2 mV s ⁻¹ | 47 |
| Ni(OH) ₂ thin film | 6 M KOH | 70.6 mF cm ⁻² at 2 mV s ⁻¹ | 17 |
| MnO ₂ -CNT film | 0.5 M K ₂ SO ₄ | 100 mF cm ⁻² at 10 mV s ⁻¹ | 7 |
| C nanoparticles/MnO ₂ nanorods | 0.1 M Na ₂ SO ₄ | 109 mF cm ⁻² at 5 mV s ⁻¹ | 8 |
| Hydrogenated ZnO/MnO ₂ | 0.5 M Na ₂ SO ₄ | 139 mF cm ⁻² at 1 mA cm ⁻² | 48 |
| CuO film on ITO-coated glass | 1 M Na ₂ SO ₄ | 2.7 F g ⁻¹ at 20 mV s ⁻¹ | 49 |
| CuO nanoribbons | 6 M KOH | 89 F g ⁻¹ at 4 A g ⁻¹ | 50 |
| O-deficient Fe ₂ O ₃ nanorods | 3 M LiCl | 89 F g ⁻¹ at 0.5 mA cm ⁻² | 38 |
| RGO/Cu ₂ O composite film | 1 M KOH | 98.5 F g ⁻¹ at 1 A g ⁻¹ | 51 |
| Mesoporous WO _{3-x} /C composite | 2 M H ₂ SO ₄ | 103 F g ⁻¹ at 1 mV s ⁻¹ | 52 |
| MnMoO ₄ /CoMoO ₄ nanowires | 2 M NaOH | 134.7 F g ⁻¹ at 3 A g ⁻¹ | 37 |
| Porous MnO ₂ | 0.65 M K ₂ SO ₄ | 135 F g ⁻¹ at 2 mV s ⁻¹ | 10 |
| CuO nanosheets/SWCNT | 6 M KOH | 137.6 F g ⁻¹ at 2 mV s ⁻¹ | 34 |
| Ppy-MnO ₂ | 1 M Na ₂ SO ₄ | 141.6 F g ⁻¹ at 2 mA cm ⁻² | 53 |
| CuO nanoparticles | 1 M Na ₂ SO ₄ | 158 F g ⁻¹ at 5 mV s ⁻¹ | 54 |
| CuO nanosheets/RGO film | 6 M KOH | 163.7 F g ⁻¹ at 2 mV s ⁻¹ | 35 |
| MnO ₂ /CNTs | 1 M Na ₂ SO ₄ | 201 F g ⁻¹ at 1 A g ⁻¹ | 55 |
| RGO/Fe ₂ O ₃ nanotubes | 1 M Na ₂ SO ₄ | 215 F g ⁻¹ at 2.5 mV s ⁻¹ | 56 |

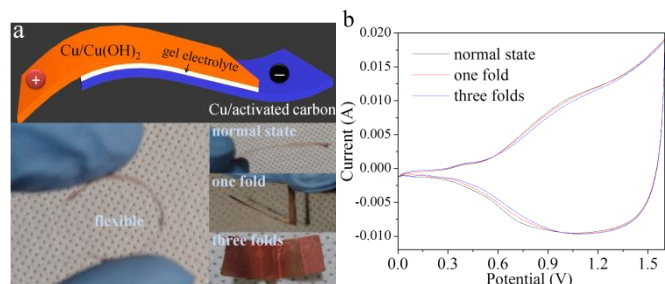


Fig. 6 (a) Graphic and photographic illustrations of flexible and foldable $\text{Cu}(\text{OH})_2//\text{AC}$ solid-state ASC. (b) CV curves of the ASC under different folding states.

Recently, solid-state flexible power sources are attracting much attention because of their potential applications in roll-up displays, artificial electronic skin, wearable electronics, etc. To further evaluate 3-D $\text{Cu}(\text{OH})_2$, we assembled solid-state ASC by using 1800 s $\text{Cu}(\text{OH})_2$ as the positive electrode, activated carbon (AC) pasted on the Cu foil as the negative electrode and PVA/KOH as the gel electrolyte, as illustrated in Fig. 6a, which also demonstrates high flexibility of the device. Fig. 6b shows CV profiles of this solid-state ASC bended to different states, i.e., normal state, one fold, and three folds. The photographs and demonstrations of these bending states are shown in the inset of Fig. 6a and Fig. S8. No noticeable change could be observed even when the ASC device is bended to three folds, indicating the great robustness of this device.

Fig. 7a shows GCD curves of this ASC under a potential cutoff of 0–1.6 V at different current densities on the basis of the total mass of both positive and negative active materials. The capacitances at 4, 10 and 20 A g^{-1} are 26.4, 19.4 and 13.7 F g^{-1} , respectively. It is seen that the redox characteristics of this ASC are not as evident as those of $\text{Cu}(\text{OH})_2$, which results from the synergistic integration of pseudocapacitive $\text{Cu}(\text{OH})_2$ and EDLC AC. Remarkably, this ASC exhibits great reversibility and very high coulombic efficiencies (> 97% through all current densities) from these GCD curves. The cycling stability of this ASC was also tested (Fig. S9). We find that this ASC can achieve a capacitance retention of nearly 90% after 5000 cycles, implying excellent stability. Ragone plots of $\text{Cu}(\text{OH})_2//\text{AC}$ solid-state ASC are displayed in Fig. 7b. It is noted that the volumes of two Cu foil current collectors and the gel electrolyte are taken into account into the total volume of the ASC. Under a high power density of 1253 mW cm^{-3} , this ASC delivers a high energy density of 3.68 mWh cm^{-3} . When the power density is increased to 5314 mW cm^{-3} with the discharging time being ~ 0.5 s, the energy density still remains at 0.73 mWh cm^{-3} . Such performances are much better than other state-of-art ASCs^{38–42} (e.g., 0.41 mWh cm^{-3} at 50 mW cm^{-3} for $\text{MnO}_2//\text{Fe}_2\text{O}_3$ ASC,³⁸ 1.9 mWh cm^{-3} at 40 mW cm^{-3} for $\text{MoS}_2//\text{RGO}/\text{RGO}$ ASC⁴²) and Li thin-film battery,¹ as compared in Fig. 7b. To verify the scalability and application of our product, we also assembled 4×6 cm^2 solid-state ASCs by anodizing 4×5 cm^2 Cu slices. The photograph of this ASC is shown in Fig. S10, in comparison with a 1×4 cm^2 device studied in the previous section. Two of these large ASC devices were connected in series to compose a tandem device. Up to 26 light-emitting diodes (LEDs) can be lighted up by the tandem device (see the supplementary video), demonstrating the potential of this device in practical high-power energy storage applications.

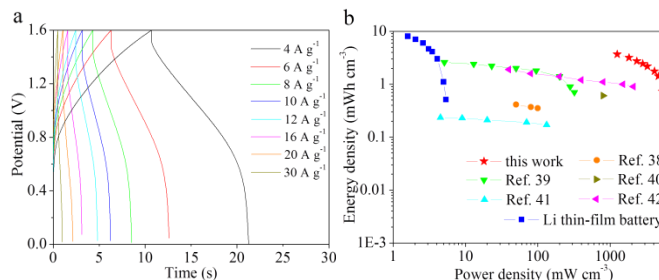


Fig. 7 (a) GCD profiles of $\text{Cu}(\text{OH})_2//\text{AC}$ solid-state ASC at different current densities. (b) Ragone plots of energy density vs. power density for our ASC in comparison with other state-of-art ASCs and Li thin-film battery.

Conclusions

In summary, we have developed a facile and scalable one-step process to anodically grow 3-D $\text{Cu}(\text{OH})_2$ nanoporous nanorods on the Cu foil, and demonstrated that the $\text{Cu}(\text{OH})_2/\text{Cu}$ foil can be used directly as a binder-free electrode for supercapacitors. The unique morphology of the nanoporous nanorods provides sufficient active sites for redox reactions and transport routes for electrolyte ions. The $\text{Cu}(\text{OH})_2$ delivers a high capacitance of 213 mF cm^{-2} or 260 F g^{-1} , together with superior rate capability and excellent long-term cyclability. Solid-state asymmetric supercapacitors are assembled using the $\text{Cu}(\text{OH})_2$ as the positive electrode and activated carbon as the negative electrode, exhibiting high energy and power densities as well as high flexibility, good foldability and excellent cycling stability. These results suggest that the $\text{Cu}(\text{OH})_2$ electrode may provide a low-cost and effective solution for future high performance supercapacitors.

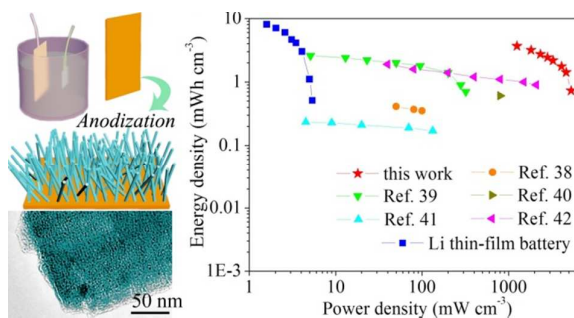
Acknowledgements

This work was supported by Research Grants Council of Hong Kong (General Research Fund, No. 417012, GRC-NSFC, No. N_CUHK450/13, and TRS, No. T23-407/13-N).

References

- Z. S. Wu, K. Parvez, X. Feng and K. Müllen, *Nat. commun.*, 2013, **4**, 2487–2494.
- L. L. Zhang and X. S. Zhao, *Chem. Soc. Rev.*, 2009, **38**, 2520–2531.
- W. Gao, N. Singh, L. Song, Z. Liu, A. L. Reddy, L. G. R. Vajtai, Q. Zhang, B. Wei and P. M. Ajayan, *Nat. Nano.*, 2011, **6**, 496–500.
- J. Chen, K. Sheng, P. Luo, C. Li and G. Shi, *Adv. Mater.*, 2012, **24**, 4569–4573.
- G. Wang, L. Zhang and J. Zhang, *Chem. Soc. Rev.*, 2012, **41**, 797–828.
- M. Armand, F. Endres, D. R. MacFarlane, H. Ohno and B. Scrosati, *Nat. Mater.*, 2009, **8**, 621–629.
- T. M. Higgins, D. McAteer, J. C. Coelho, B. M. Sanchez, Z. Gholamvand, G. Moriarty, N. McEvoy, N. C. Bemer, G. S. Duesberg, V. Nicolosi and J. N. Coleman, *ACS nano*, 2014, **8**, 9567–9579.
- L. Yuan, X. H. Lu, X. Xiao, T. Zhai, J. Dai, F. Zhang, B. Hu, X. Wang, L. Gong, J. Chen, C. Hu, Y. Tong, J. Zhou and Z. L. Wang, *ACS nano*, 2012, **6**, 656–661.
- Z. Yu, B. Duong, D. Abbitt and J. Thomas, *Adv. Mater.*, 2013, **25**,

- 3302-3306.
- 10 A. Gambou-Bosca and D. Belanger, *J. Mater. Chem. A*, 2014, **2**, 6463-6473.
- 11 S. Wu, W. Chen and L. Yan, *J. Mater. Chem. A*, 2014, **2**, 2765-2772.
- 12 R. Zou, K. Xu, T. Wang, G. He, Q. Liu, X. Liu, Z. Zhang and J. Hu, *J. Mater. Chem. A*, 2013, **1**, 8560-8566.
- 13 C. Yuan, J. Li, L. Hou, X. Zhang, L. Shen and X. W. D. Lou, *Adv. Funct. Mater.*, 2012, **22**, 4592-4597.
- 14 Y. Zhu, Z. Wu, M. Jing, H. Hou, Y. Yang, Y. Zhang, X. Yang, W. Song, X. Jia and X. Ji, *J. Mater. Chem. A*, 2015, **3**, 866-877.
- 15 X. Lu, D. Wu, R. Li, Q. Li, S. Ye, Y. Tong and G. Li, *J. Mater. Chem. A*, 2014, **2**, 4706-4713.
- 16 J. Chen, J. Xu, S. Zhou, N. Zhao and C.-P. Wong, *Nano Energy*, 2015, **15**, 719-728.
- 17 Y. Yang, L. Li, G. Ruan, H. Fei, C. Xiang, X. Fan and J. M. Tour, *ACS nano*, 2014, **8**, 9622-9628.
- 18 H. B. Li, M. H. Yu, F. X. Wang, P. Liu, Y. Liang, J. Xiao, C. X. Wang, Y. X. Tong and G. W. Yang, *Nat. Commun.*, 2013, **4**, 1894-1900.
- 19 L. Li, J. Xu, J. Lei, J. Zhang, F. McLamou, Z. Wei, N. Li and F. Pan, *J. Mater. Chem. A*, 2015, **3**, 1953-1960.
- 20 L. Wang, C. Lin, F. Zhang and J. Jin, *ACS nano*, 2014, **8**, 3724-3734.
- 21 J. Xu, S. Gai, F. He, N. Niu, P. Gao, Y. Chen and P. Yang, *J. Mater. Chem. A*, 2014, **2**, 1022-1031.
- 22 W. Chen, C. Xia and H. N. Alshareef, *ACS nano*, 2014, **8**, 9531-9541.
- 23 J. Xiao, L. Wan, S. Yang, F. Xiao and S. Wang, *Nano Lett.*, 2014, **14**, 831-838.
- 24 H. C. Chen, J. J. Jiang, L. Zhang, D. D. Xia, Y. D. Zhao, D. Q. Guo, T. Qi and H. Z. Wan, *J. Power Sources*, 2014, **254**, 249-257.
- 25 R. Zou, Z. Zhang, M. F. Yuen, J. Hu, C. S. Lee and W. Zhang, *Sci. Rep.*, 2015, **5**, 7862-7868.
- 26 J. Wang, D. Chao, J. Liu, L. Li, L. Lai, J. Lin and Z. Shen, *Nano Energy*, 2014, **7**, 151-160.
- 27 S. Li, D. Huang, J. Yang, B. Zhang, X. Zhang, G. Yang, M. Wang and Y. Shen, *Nano Energy*, 2014, **9**, 309-317.
- 28 Y. Zhou, H. Xu, N. Lachman, M. Ghaffari, S. Wu, Y. Liu, A. Ugur, K. Gleason, B. L. Wardle and Q. M. Zhang, *Nano Energy*, 2014, **9**, 176-185.
- 29 Y. Shi, L. Pan, B. Liu, Y. Wang, Y. Cui, Z. Bao and G. Yu, *J. Mater. Chem. A*, 2014, **2**, 6086-6091.
- 30 K. V. Gurav, U. M. Patil, S. W. Shin, G. L. Agawane, M. P. Suryawanshi, S. M. Pawar, P. S. Patil, C. D. Lokhande and J. H. Kim, *J. Alloy. Compd.*, 2013, **573**, 27-31.
- 31 S. Zheng, J. Hu, L. Zhong, W. Song, L. Wan and Y. Guo, *Chem. Mater.*, 2008, **20**, 3617-3622.
- 32 C. Z. Yuan, J. Y. Li, L. R. Hou, X. G. Zhang, L. F. Shen and X. W. Lou, *Adv. Funct. Mater.*, 2012, **22**, 4592-4597.
- 33 C. Guan, J. P. Liu, C. W. Cheng, H. X. Li, X. L. Li, W. W. Zhou, H. Zhang and H. J. Fan, *Energ. Environ. Sci.*, 2011, **4**, 4496-4499.
- 34 Y. Liu, H. Huang and X. Peng, *Electrochim. Acta*, 2013, **104**, 289-294.
- 35 Y. Liu, Y. Ying, Y. Mao, L. Gu, Y. Wang and X. Peng, *Nanoscale*, 2013, **5**, 9134-9140.
- 36 Y. Yang, H. Fei, G. Ruan, C. Xiang and J. M. Tour, *Adv. Mater.*, 2014, **26**, 8163-8168.
- 37 L. Q. Mai, F. Yang, Y. L. Zhao, X. Xu, L. Xu and Y. Z. Luo, *Nat. Commun.*, 2011, **2**, 381-385.
- 38 X. Lu, Y. Zeng, M. Yu, T. Zhai, C. Liang, S. Xie, M. S. Balogun and Y. Tong, *Adv. Mater.*, 2014, **26**, 3148-3155.
- 39 C. Zhou, Y. Zhang, Y. Li and J. Liu, *Nano Lett.*, 2013, **13**, 2078-2085.
- 40 X. Lu, M. Yu, T. Zhai, G. Wang, S. Xie, T. Liu, C. Liang, Y. Tong and Y. Li, *Nano Lett.*, 2013, **13**, 2628-2633.
- 41 W. Zilong, Z. Zhu, J. Qiu and S. Yang, *J. Mater. Chem. C*, 2014, **2**, 1331-1336.
- 42 G. Sun, X. Zhang, R. Lin, J. Yang, H. Zhang and P. Chen, *Angew. Chem., Int. Ed.*, 2015, **54**, 4651-4656.
- 43 M. Salari, S. H. Aboutalebi, K. Konstantinov and H. K. Liu, *Phys. Chem. Chem. Phys.*, 2011, **13**, 5038-5041.
- 44 R. Li, X. Ren, F. Zhang, C. Du and J. Liu, *Chem. Commun.*, 2012, **48**, 5010-5012.
- 45 J. H. Kim, S. H. Kang, K. Zhu, J. Y. Kim, N. R. Neale and A. J. Frank, *Chem. Commun.*, 2011, **47**, 5214-5216.
- 46 X. Lu, T. Zhai, X. Zhang, Y. Shen, L. Yuan, B. Hu, L. Gong, J. Chen, Y. Gao, J. Zhou, Y. Tong and Z. L. Wang, *Adv. Mater.*, 2012, **24**, 938-944.
- 47 J. Yan, E. Khoo, A. Sumboja and P. S. Lee, *ACS nano*, 2010, **4**, 4247-4255.
- 48 P. Yang, X. Xiao, Y. Li, Y. Ding, P. Qiang, X. Tan, W. Mai, Z. Lin, W. Wu, T. Li, H. Jin, P. Liu, J. Zhou, C. P. Wong and Z. L. Wang, *ACS nano*, 2013, **7**, 2617-2626.
- 49 C. Zhu and M. J. Panzer, *Chem. Mater.*, 2014, **26**, 2960-2966.
- 50 B. Heng, C. Qing, D. Sun, B. Wang, H. Wang and Y. Tang, *RSC Adv.*, 2013, **3**, 15719-15726.
- 51 X. Dong, K. Wang, C. Zhao, X. Qian, S. Chen, Z. Li, H. Liu and S. Dou, *J. Alloy. Compd.*, 2014, **586**, 745-753.
- 52 C. Jo, J. Hwang, H. Song, A. H. Dao, Y.-T. Kim, S. H. Lee, S. W. Hong, S. Yoon and J. Lee, *Adv. Funct. Mater.*, 2013, **23**, 3747-3754.
- 53 A. Bahloul, B. Nessark, E. Briot, H. Groult, A. Manger, K. Zaghbi and C. M. Julien, *J. Power Sources*, 2013, **240**, 267-272.
- 54 A. Pendashteh, M. S. Rahmanifar and M. F. Mousavi, *Ultrason. Sonochem.*, 2014, **21**, 643-652.
- 55 L. Li, Z. A. Hu, N. An, Y. Y. Yang, Z. M. Li and H. Y. Wu, *J. Phys. Chem. C*, 2014, **118**, 22865-22872.
- 56 K. K. Lee, S. Deng, H. M. Fan, S. Mhaisalkar, H. R. Tan, E. S. Tok, K. P. Loh, W. S. Chin and C. H. Sow, *Nanoscale*, 2012, **4**, 2958-2961.



3-D Cu(OH)₂ nanoporous nanorods are fabricated by a facile and scalable one-step anodization method for high-performance binder-free solid-state supercapacitors.